

# Development of fast, simultaneous and multi-technique scanning hard X-ray microscopy at Synchrotron Soleil

Kadda Medjoubi,<sup>a\*</sup> Nicolas Leclercq,<sup>a</sup> Florent Langlois,<sup>a</sup> Alain Buteau,<sup>a</sup> Stephane L e,<sup>a</sup> St ephane Poirier,<sup>a</sup> Pascal Merc ere,<sup>a</sup> Marie Catherine Sforna,<sup>b</sup> Cameron M. Kewish<sup>a</sup> and Andr ea Somogyi<sup>a</sup>

<sup>a</sup>Synchrotron Soleil, BP 48, Saint-Aubin, 91192 Gif sur Yvette, France, and <sup>b</sup>Equipe de Geobiosph ere Actuelle et Primitive, Institut de Physique du Globe de Paris, Sorbonne Paris Cit e, Universit e Paris Diderot, UMR 7154 CNRS, 1 rue Jussieu, Paris 75005, France.  
E-mail: kadda.medjoubi@synchrotron-soleil.fr

A distributed fast-acquisition system for synchronized multi-technique experiments is presented, in which the collection of metadata and the asynchronous merging of large data volumes from multiple detectors are managed as part of the data collection process. This fast continuous scanning scheme, named FLYSCAN, enables measurement of microscopy data on a timescale of milliseconds per pixel. Proof-of-principle multi-technique experiments, namely scanning X-ray fluorescence spectrometry combined with absorption, differential phase contrast and dark-field imaging, have been performed on biological and geological samples.

**Keywords:** X-ray multi-technique imaging; scanning hard X-ray nanoprobe; continuous scan; phase contrast; differential phase contrast; dark field; fluorescence microprobe.

## 1. Introduction

Scanning hard X-ray nanoprobe techniques provide powerful tools for probing specimens down to the nanometer scale with high elemental and structural sensitivity (Kaulich *et al.*, 2011). The sample is raster-scanned in a focused X-ray beam, while the transmitted beam and/or secondary emission are recorded at each sample position. Scanning hard X-ray imaging is well suited to multimodal experiments since complementary contrast information can be easily collected by introducing multiple detectors around the sample. For instance, X-ray fluorescence (XRF) spectrometry reveals the elements contained in the sample, and is often combined with X-ray absorption spectroscopy to give information on the chemical state. The detection of the transmitted X-rays by a two-dimensional array detector provides data for scanning transmission X-ray microscopy (STXM); that is, bright-field, dark-field and differential phase contrast images are obtained from the same recorded dataset. The combination of simultaneous and complementary imaging modes provides comprehensive and quantitative information about the structural and chemical distribution within the sample (Kaulich *et al.*, 2011; Kosior *et al.*, 2012).

The use of hard X-rays in scanning nanoprobe has several advantages owing to the large penetration depth. This permits several tens of  $\mu\text{m}$ -thick samples and buried structures to be studied with limited sample preparation. Moreover, high

(parts per billion, p.p.b.) sensitivity can be achieved by XRF imaging for a large range of elements, by exploiting the excitation of the *K*- and *L*-shell electrons.

During recent years significant technical progress has been reported in hard X-ray scanning microscopy through developments in focusing optics, sample positioning, detector technology and imaging methodologies, with a direct benefit for a wide range of scientific applications. State-of-the-art focusing devices (Vila-Comamala *et al.*, 2011; Mimura *et al.*, 2009; Yan *et al.*, 2010, 2011; Boye *et al.*, 2009) have demonstrated diffraction-limited beam focusing to below 10 nm. High-accuracy nano-positioning stages have become available for nanometer-precision sample positioning (Holler *et al.*, 2012).

High-sensitivity and fast-readout detectors are crucial for the implementation of fast scanning techniques. Indeed, high-solid-angle energy-dispersive detectors (Ryan *et al.*, 2009) have been developed for high-speed XRF mapping. Furthermore, the development of different types of fast position-sensitive detectors and their integration in fast scanning experiments has been reported recently (Hornberger *et al.*, 2008; Menzel *et al.*, 2010). Pixelated photon-counting detectors enable fast readout, high dynamic range, one-pixel spatial resolution and noiseless detection, which make them especially well suited to scanning imaging. As signal-to-noise ratio is only limited by Poisson statistics in these noiseless photon-counting detectors, good image quality can be achieved even

at low exposure. Consequently, an image can be obtained with significantly reduced dose to the sample and with a reduced total acquisition time.

These technical developments have fostered the implementation of fast-scanning multi-technique nanoprobe methods, where a sample is scanned in continuous motion, while the detector signal is recorded for every pixel of the resulting image. Recent scanning imaging set-ups are often suffering from the present limitations resulting from the use of slow-pixel-rate acquisition systems (as discussed by Lombi *et al.*, 2011), which are recently being tackled by single technique systems (Ryan *et al.*, 2009). However, the implementation of multi-technique fast scanning with millisecond-range dwell time per pixel is still a technical challenge. This technique, where full-frame two-dimensional transmission data, incident-beam intensity monitors, sample positions as measured by motor encoders and full XRF spectra are recorded in parallel for every pixel, is a major requirement on state-of-the-art beamlines. This type of scanning with fast two-dimensional pixel array detectors and fluorescence spectrometers results in a more than few hundred megabytes per second of data throughput, placing heavy demands on the beamline computing and network infrastructure. Acquiring such a data set to produce a megapixel image of a sample results in a recorded data volume of the order of a hundred gigabytes, which can grow substantially with the use of pixelated XRF detectors that collect several hundred spectra per image pixel (Ryan *et al.*, 2009). The extension of these techniques, *e.g.* to tomography imaging (three-dimensional) or XANES imaging/tomography (three-dimensional/four-dimensional), results in another few orders of magnitude increase in the data volume. This data volume must be processed quickly for on-line inspection of the data quality, and stored for detailed off-line processing. Moreover, the process of storing this data must not limit the speed of acquisition or the synchronicity of the data recorded.

The Nanoscopium beamline (Somogyi *et al.*, 2011), under construction at Synchrotron Soleil, is dedicated to such multi-technique scanning nanoprobe imaging in the hard X-ray energy range 5–25 keV. Both continuous fast scanning with millisecond dwell times and nanometre-precision step-scan mode operation are required for multiscale imaging; that is, imaging large fields of view with moderate spatial resolution and sensitivity, followed by high spatial resolution and high sensitivity mapping of small volumes of interest. The FLYSCAN project has been developed at Soleil to tackle the technical challenges associated with implementing this fast continuous scanning mode on this

beamline and then to transfer the FLYSCAN scheme to other Soleil beamlines. This paper presents the first results of multi-modal imaging obtained with the prototype FLYSCAN architecture on the Metrologie beamline of Soleil (Idir *et al.*, 2010).

## 2. The architecture of the FLYSCAN

The FLYSCAN project was designed to allow a distributed fast acquisition system for synchronized multi-technique experiments. The related hardware and software architecture was developed in a generic way, based on standard software and hardware components used at Soleil, so that it can be easily implemented at other beamlines.

The FLYSCAN architecture is schematically illustrated in Fig. 1. The data collection ‘front end’ is a synchronous process, in which data are acquired simultaneously from several independent sources which include detectors and encoders. Each acquisition subsystem is independent, and their acquisition is synchronized by a common hardware trigger. Each component of the acquisition chain is controlled individually by a dedicated TANGO device (<http://www.tango-controls.org/>) through a distributed TCP/IP network. This allows a remote access to their configuration. Each device is configured with independent parameters, for example exposure time or frame rate, scanning range, step size, scan geometry (*i.e.* uni- or bi-directional raster scan), and triggering sequence, through a sequencing execution tool such as MATLAB (The MathWorks, Natick, MA, USA), Python (<http://www.python.org/>) or Passerelle workflow engine (Abeillé *et al.*, 2007). This distributed architecture enables a flexible and modular

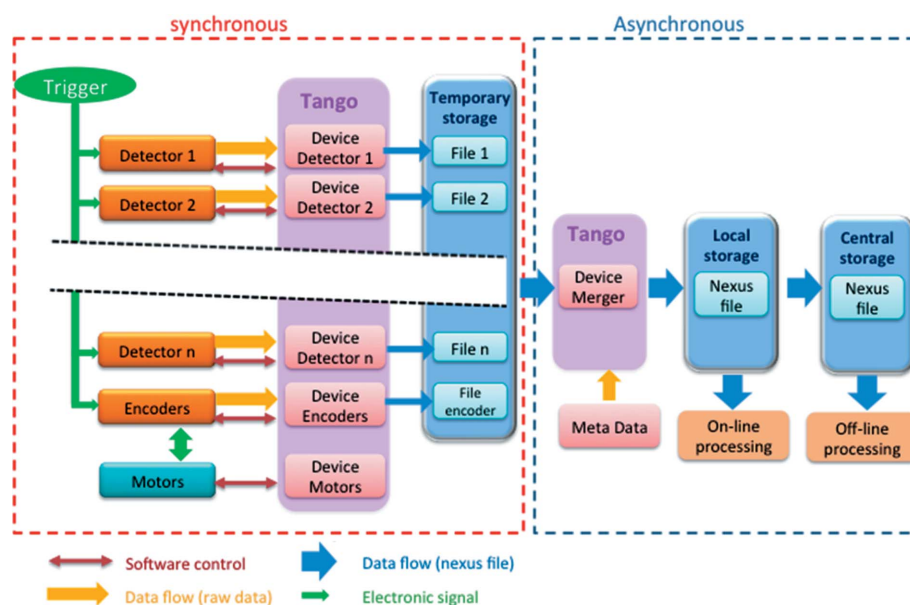


**Figure 1** Principle of the FLYSCAN architecture. Detectors and encoders, triggered with a common hardware signal, are controlled by their own TANGO device. The output data of each device is recorded, in a synchronous way, in a separate temporary file in a dedicated storage space. An asynchronous process collects these temporary data and merges them into a unique NeXus format file, which can be read out during the acquisition process making online processing possible. This final file is then copied to the central data storage.

operation. For example, an acquisition subsystem can be easily added or removed from the measurement chain without any modification of the existing acquisition software.

Each TANGO device collects raw data from its detector in response to the trigger signal, and stores it temporarily in a local temporary storage space. The time response of each separate device to the trigger signal is submicrosecond, which is low compared with the dwell time. At the end of each trigger sub-sequence, *e.g.* after each line of a two-dimensional scan, the raw files are merged into a temporary NeXus (HDF5 compatible) file (Poirier *et al.*, 2009). In order to repeat a sequence of synchronous acquisitions as fast as possible, the overall data handling is an asynchronous process. The DataMerger TANGO device monitors the temporary storage. When all the temporary files corresponding to one trigger sub-sequence are available, DataMerger appends them to a single NeXus file on the local storage system of the beamline. Metadata, describing the context of the experiments, such as scan parameters, sample identifier, beamline parameters and timestamp, are also included in the data file. The hierarchical NeXus format facilitates data processing, because the data from each acquisition subsystem are merged together according to the trigger sub-sequence. The merged NeXus file can be read during acquisition which allows on-line data processing and visualization. When the merging of the scan is completed, the final NeXus file is copied and stored in a central storage, where it is available for off-line analysis.

### 3. Experimental

#### 3.1. Prototype development at the Metrologie beamline

To test and demonstrate the FLYSCAN scheme, a prototype microprobe was installed at the Metrologie bending-magnet beamline of Soleil (Fig. 2). The monochromatic beam of 14 keV was focused by a 900 nm-thick tungsten Fresnel zone plate with 240  $\mu\text{m}$  diameter and 100 nm outermost zone width (Charalambous, 2011). A 25  $\mu\text{m}$ -diameter central stop and a

20  $\mu\text{m}$  order-sorting aperture were used to block the radiation transmitted and diffracted into higher orders by the zone plate, allowing only the first-order focus to illuminate the sample. The focus was measured to be approximately 1.6  $\mu\text{m}$  in diameter (FWHM), using the knife-edge scan method (Hayakawa *et al.*, 1989). The focus size was due to the demagnification of the bending-magnet source. The flux measured in the focused beam was  $\sim 6 \times 10^6$  photons  $\text{s}^{-1}$ . The sample was mounted on a two-dimensional translation stage with the scan axes horizontal and vertical perpendicular to the X-ray beam direction. The positions of the motor stages were given by the counting of TTL pulses provided by the incremental encoders. The counting was performed using a PXI 6602 counter board from National Instruments (<http://www.ni.com/>).

The transmitted beam was recorded with a photon-counting pixel detector, a single-module XPAD (Medjoubi *et al.*, 2010), placed 4.41 m behind the sample. The detector consisted of a 1.5 cm  $\times$  7 cm monolithic silicon sensor (500  $\mu\text{m}$  thick) bump-bonded to electronic chips. It contained 560  $\times$  120 pixels with 130  $\mu\text{m}$  pixel size each. A full image can be read out in 1.6 ms, through a fast data acquisition system resulting in a maximum frame rate of 640 Hz. The acquisition of each image was started with an external trigger.

A silicon drift detector with 80 mm<sup>2</sup> active area (VITUS H80, KETEK GmbH) was mounted at 90° to the incident X-ray beam to measure the X-ray fluorescence emitted by the sample. A high-speed digital multichannel analyzer (xMAP, XIA LLC) was used in double-buffering memory mode, allowing continuous collection of XRF spectra. Indeed, in this mode, readout and acquisition are supported simultaneously.

A thin silicon photodiode (AXUV36, IRD inc) was placed upstream of the zone plate, to record the incident beam intensity. The output current from the photodiode was read by a current-to-voltage amplifier, followed by analog-to-digital converter (DAQ-2005, ADLINK).

Two-dimensional large STXM scans were carried out, with a small food moth as a sample, in which the sample was moved continuously along the horizontal axis, while in parallel the incoming beam intensity, a transmission image and the sample stage encoder positions were recorded in response to each trigger flow from the FLYSCAN architecture. A second counter card (PXI 6602) was configured as a pulse generator and used to generate the master trigger for synchronizing the data acquisition. The minimum achievable trigger period is determined by the readout time of the slowest detector of the chain, in this case the 1.6 ms readout time of the XPAD. The flux available from the bending magnet required a trigger period of 12 ms in these experiments. The motor speed was chosen to match the 1.6  $\mu\text{m}$  effective horizontal pixel size

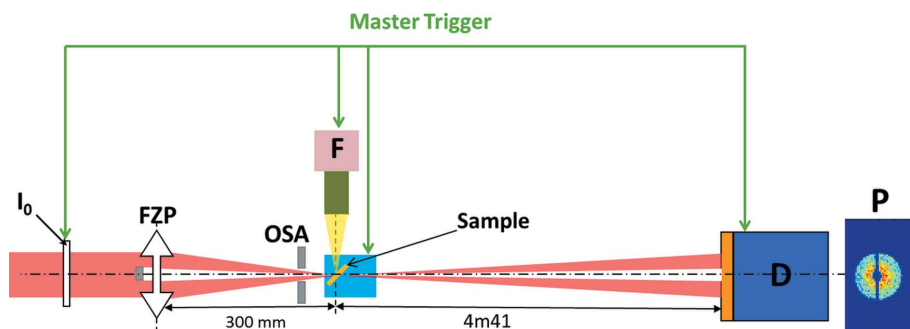


**Figure 2**

Schematic illustration of the test measurement geometry; monochromatic X-rays of energy 14 keV are incident on a Fresnel zone plate (FZP), whose first-order focus, selected by an order-sorting aperture (OSA), illuminates a sample aligned at 45° to the beam. A TTL pulse (master trigger) triggers the simultaneous recording of: the incident beam intensity with a thin silicon photodiode ( $I_0$ ), the transmitted beam intensity with a pixel array detector (D) (P: recorded transmission pattern), the emitted fluorescence with an energy-dispersive detector (F), and the encoder positions of the sample scanning stage.

of the map. After each scan line of 1000 measurements, the sample was stepped in the vertical direction by 2  $\mu\text{m}$ , to build up a scan of 1000 lines. To minimize the time lost owing to movement between measurements, the sample was scanned in a bidirectional (raster ‘zigzag’) mode. The total acquisition time was 4.5 h, which includes overheads of a few seconds at each end of line. By comparison, a step-scan with the same number of points and including additional overheads for settling time and software protocol between measurements would take several days. The final 140 Gb NeXus data file contained one million XPAD frames, one million intensity monitor values and two million encoder positions.

To demonstrate the combination of STXM and XRF imaging, a similar two-dimensional scan was carried out using a polished section of a fossilized stromatolite, wherein the intensity monitor, XPAD and encoders were read out at the same time as the XRF spectra. A mapping of  $500 \times 400$  pixels with  $1.6 \times 2 \mu\text{m}$  effective pixel size was performed with a trigger period of 58 ms, determined by the detection limit of the XRF signals.

### 3.2. Data processing

Transmission contrast, differential phase contrast (DPC) and dark-field images are calculated from the images of the transmitted defocused beam acquired with the XPAD detector. For each pixel of the map, the transmission is calculated by the numerical integration of the illumination pattern and is normalized by the value obtained without object.

DPC in both horizontal and vertical directions is obtained by the measurement of the deflection of the beam in each pixel of the map.

The refraction angle obtained in each pixel is related to the phase gradient by the formula (Mukaide *et al.*, 2009)

$$\frac{\partial\varphi(x, y)}{\partial x \text{ or } y} = \frac{2\pi}{\lambda} \theta_{x \text{ or } y} \quad (1)$$

where  $\varphi(x, y)$  is the phase,  $\theta_{x \text{ or } y}$  is the refraction angle along the horizontal,  $x$ , or vertical,  $y$ , directions and  $\lambda$  is the wavelength. As such, phase retrieval can be performed from the DPC images [*cf.* equation (2)]. This yields the complete knowledge of the specimen’s complex-valued optical X-ray transmission function.

Dark-field contrast is related to the scattered X-rays from the sample. This imaging mode probes density fluctuations on a length-scale smaller than the illuminated area (Menzel *et al.*, 2010). Dark field is evaluated by integrating the intensity of all pixels located outside the first order of the zone plate.

XRF imaging is obtained from the analysis of the fluorescence spectrum measured in each pixel of the scan. Peak area integrals were used to obtain elemental distribution maps. Unlike the differential phase contrast, the transmission, dark field and XRF are sensitive to temporal fluctuation of incident beam intensity and, therefore, were corrected using the recorded intensity monitor values.

Motor acceleration, deceleration, speed variation and backlash may significantly influence the image quality. These effects were corrected using the registered encoder positions. The images were rescaled by using a cubic spline interpolation with MATLAB.

All of the above-described data processing was performed on-line allowing for (*in situ*) visualization of the scanning process.

The phase retrieval is part of the off-line processing. The technique used is the Fourier integration of the complex sum of the horizontal and vertical gradient phase images as described in the following equation (Kottler *et al.*, 2007; Arnison *et al.*, 2004),

$$\varphi(x, y) = \text{Re} \left( \mathcal{F}^{-1} \left\{ \frac{\mathcal{F} \left[ \frac{\partial\varphi(x, y)}{\partial x} + i \frac{\partial\varphi(x, y)}{\partial y} \right]}{2\pi i(u + iv)} \right\} \right), \quad (2)$$

where  $\text{Re}$  denotes the real part,  $\mathcal{F}$  and  $\mathcal{F}^{-1}$  are the direct and inverse Fourier transform, respectively, and  $u$  and  $v$  are the coordinates in reciprocal space.

Before the numerical integration, mirror imaging processing was applied on both DPC images to reduce the error from edge discontinuity effects (Mukaide *et al.*, 2009). In addition, numerical divergence is avoided by setting to zero the DC-frequency in the reciprocal space.

## 4. Results

Fig. 3 shows the complementary contrast information obtained with the large scan of the moth sample. As expected, in low-absorption regions (Fig. 3*a*) a strong differential phase contrast (Fig. 3*b*) is observed. For instance, the antenna of the moth produces a lateral shift at the detector plane of about half a pixel, which corresponds to a refraction angle of 15  $\mu\text{rad}$ . The noise, extracted from a featureless region outside the object, is evaluated to 0.95  $\mu\text{rad}$  (RMS), which is in agreement with the calculated error. Indeed, the error of the measured refraction angle according to Menzel *et al.* (2010) can be approximated by  $N_A/I^{1/2}$ , with  $N_A$  the numerical aperture of the focusing optic and  $I$  the total number of detected photons, and gives  $\sim 1 \mu\text{rad}$  (RMS). This confirms that experimental error is determined by the beam statistics and the measurement geometry. The signal-to-noise ratio of the DPC image is one order of magnitude larger than that of the transmission image.

Fig. 3(*d*) represents the reconstructed phase of the specimen, which has been evaluated as described in §3.2. Indeed, cracks and cells structures are clearly visible in the eye of the moth as shown by the zoomed region in the inset. The equivalent region of the transmission image is shown in the inset of Fig. 3(*a*).

Fig. 3(*c*) shows the dark-field image of the moth. Dark field highlights variation of the electronic density at a scale below the resolution of the probe, *e.g.* in this experiment less than 1.6  $\mu\text{m}$ . As shown in Fig. 3(*c*), complementary details compared with the previous image modalities are revealed

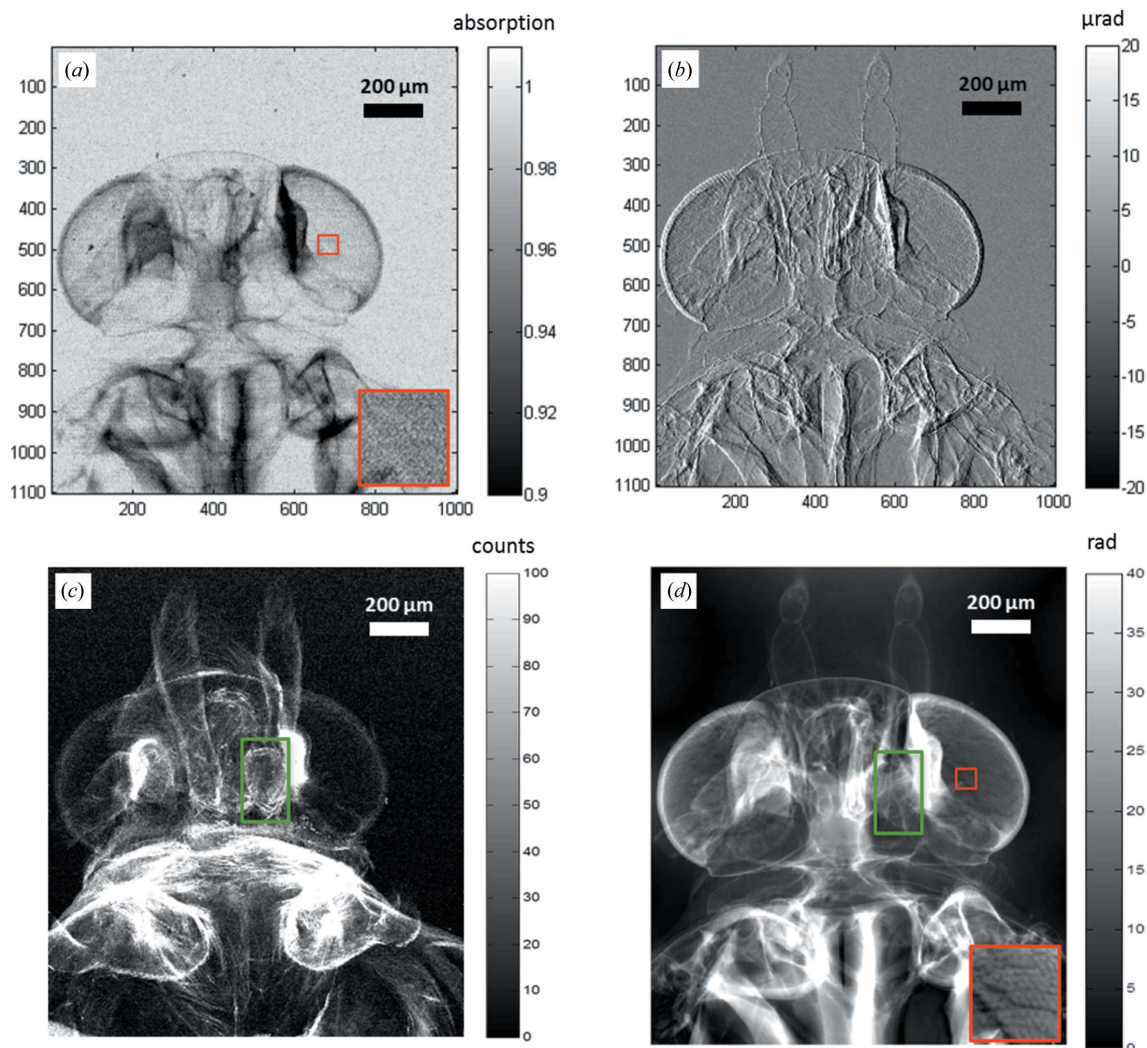


**Figure 3**

Megapixel FLYSCAN images of a moth. (a) Bright-field (absorption) image; (b) horizontal differential phase contrast; (c) dark-field (scattering strength) image; (d) quantitative phase projection reconstructed from vertical and horizontal DPC images.

indicating submicrometre structures within the eye [cf. green rectangle in Figs. 3(c) and 3(d)] and shoulder of the moth.

The potential of fast-scanning imaging with simultaneous X-ray fluorescence and STXM modes was demonstrated by measuring a stromatolite sample. The transmission, DPC, phase contrast and dark-field images are presented in Fig. 4. This stromatolite (cf. Fig. 4a), which is a bio-sedimentary layered structure, results from micro-organism activity. It consists of alternating of pure calcium carbonate layers, mixed calcium carbonate, quartz and fossilized organic matter layers, and fossilized organic matter layers. The sample was a polished 80  $\mu\text{m}$ -thick section. Study of these highly heterogeneous samples for finding structures that could indicate biological origins requires detailed, statistically significant, structural and chemical analysis at multiple length scales.

Two types of mineralogical assemblages can be identified from the transmission and DPC images [Figs. 4(b) and 4(c), respectively]. The first type, indicated by a dotted square in

Figs. 4(b) and 4(c), shows high absorption and negligible DPC contrast. It corresponds to homogeneous and dense single carbonate crystals located at the rim of the 'pure' calcite layer. The second type, located in the middle of the 'pure' calcite layer and in the mixed layers, indicated by a dotted circle, reveals significant DPC contrast variation and corresponds to polycrystalline carbonate structure. Some additional small clusters are only visible in the dark-field image (Fig. 4d). The phase map (Fig. 4e) was reconstructed from the horizontal and vertical DPC images [equation (2)] as previously discussed. The simultaneously collected Fe, Ca and Mn fluorescence maps (Fig. 5) show the difference in the chemistry of the carbonate crystals, which are pure calcite and Ca-Fe carbonate, respectively. The combination of the XRF and transmission information provides quantitative information about the elemental distribution of the specimen.

The low intensity of the recorded characteristic X-ray lines is due to the low ( $\sim 6 \times 10^6$  photons  $\text{s}^{-1}$ ) incident flux available with the test set-up. It proves the potential and feasibility

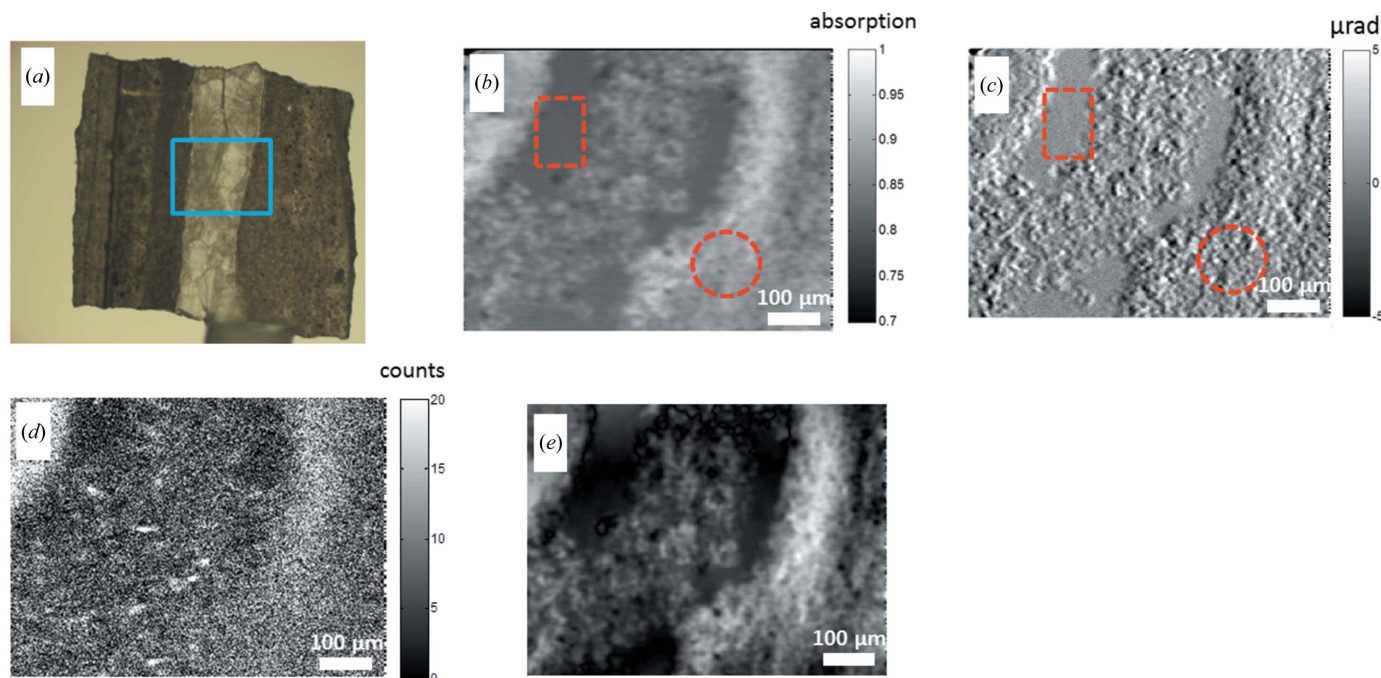


**Figure 4** FLYSCAN images of a thin section of fossilized stromatolite (*a*) (the region scanned is indicated with a rectangle); (*b*) bright-field image; (*c*) horizontal differential phase contrast; (*d*) dark-field image; (*e*) quantitative phase projection reconstructed from vertical and horizontal DPC images.

of fast XRF imaging with trace-element (part per million, p.p.m.) sensitivity at a dedicated high-flux nanoprobe beamline, such as Nanoscopium, where a  $\sim 10^{10}$ – $10^{11}$  photons  $s^{-1}$  flux is foreseen in the focused beam.

### 5. Conclusion

We present here a fast continuous scanning scheme with simultaneous synchronized multi-detection, capable of imaging with exposure times in the milliseconds-per-pixel regime. Metadata collection and asynchronous merging of the resulting high data throughput are an important part of the data collection architecture.

This prototype architecture is completely adapted to the requirements of the fast multi-technique hard-X-ray scanning nanoprobe imaging. It allows the maximum data throughput deliverable by the applied detectors to be supported, *i.e.*

200 Mbytes  $s^{-1}$ , including the data transfer, processing and storage. This will enable large field of view scans, measurement of statistically significant data sets, multi-length scale imaging, and multi-modal (tomography and XANES) imaging during a typical user experiment.

Thus, it has demonstrated the feasibility of providing fast continuous high-sensitivity scans at the future Nanoscopium beamline.

Furthermore, the FLYSCAN scheme is a general purpose ‘plug and play’ detection system. The flexible adaptation of the number and type of the detectors to the experimental needs is implemented; any detector which can be triggered by an external signal can be included in the measurement chain.

By adapting the triggering event (*e.g.* motor positions, a measured experimental value, *etc.*) and the trigger sequence, any experiment requiring synchronized multi-detector data collection can be performed by the FLYSCAN scheme. This

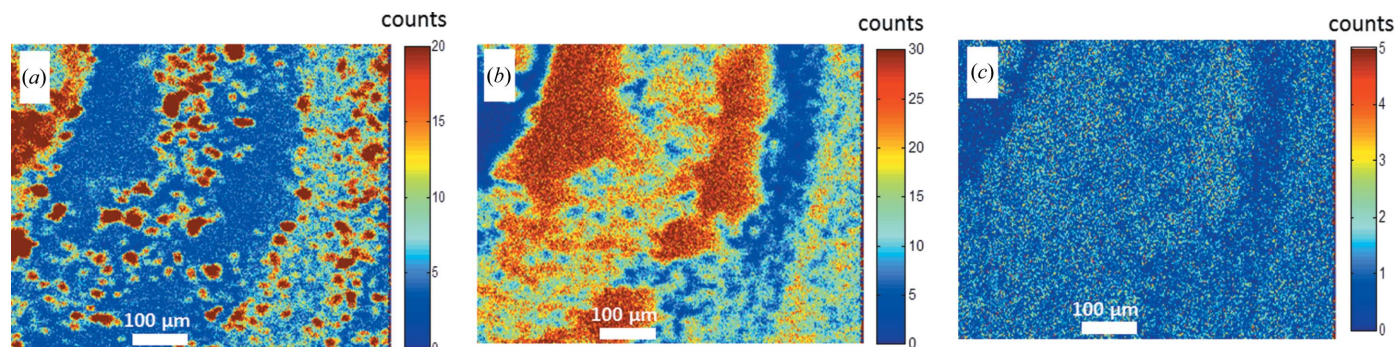


**Figure 5** Fe (*a*), Ca (*b*) and Mn (*c*) fluorescence maps of a thin section of fossilized stromatolite.

ensures its general purpose application at other Soleil beamlines in the near future.

The authors are grateful to G. Baranton and P. Da Silva from Soleil for their assistance with the synchrotron experiments, and to J. C. Clemens, F. Bompard (CPPM/CNRS) and S. Hustache (Soleil) for their support with the XPAD detector. We acknowledge V. Kaiser (ANKA/Softwareschneider GmbH) for providing the xMAP TANGO device and our colleagues from ICA/ECA from Soleil who helped us setting up the test experiments. The authors are grateful for the fruitful discussion with Andrew Thompson (Soleil). We would like to thank J. P. Samama (Soleil) for his continuous support of the FLYSCAN project.

## References

- Abeillé, G., Ounsy, M. & Buteau, A. (2007). *Proceedings of the 11th International Conference on Accelerator and Large Experimental Physics Control Systems (ICALPECS2007)*, Knoxville, Tennessee, USA, pp. 647–649.
- Arnison, M. R., Larkin, K. G., Sheppard, C. J., Smith, N. I. & Cogswell, C. J. (2004). *J. Microsc.* **214**, 7–12.
- Boye, P., Feldkamp, J. M., Patommel, J., Schwab, A., Stephan, S., Hoppe, R., Schroer, C. G., Burghammer, M., Riekkel, C., Van Der Hart, A. & Küchler, M. (2009). *J. Phys. Conf. Ser.* **186**, 012063.
- Charalambous, P. (2011). *AIP Conf. Proc.* **1365**, 65–68.
- Hayakawa, S., Lida, A. & Gohshi, Y. (1989). *Rev. Sci. Instrum.* **60**, 2452.
- Holler, M., Raabe, J., Diaz, A., Guizar-Sicairos, M., Quitmann, C., Menzel, A. & Bunk, O. (2012). *Rev. Sci. Instrum.* **83**, 073703.
- Hornberger, B., de Jonge, M. D., Feser, M., Holl, P., Holzner, C., Jacobsen, C., Legnini, D., Paterson, D., Rehak, P., Strüder, L. & Vogt, S. (2008). *J. Synchrotron Rad.* **15**, 355–362.
- Idir, M., Mercere, P., Moreno, T., Delmotte, A., Dasilva, P. & Modi, M. H. (2010). *AIP Conf. Proc.* **1234**, 485–488.
- Kaulich, B., Thibault, P., Gianoncelli, A. & Kiskinova, M. (2011). *J. Phys. Condens. Matter*, **23**, 083002.
- Kosior, E., Bohic, S., Suhonen, H., Ortega, R., Devès, G., Carmona, A., Marchi, F., Guillet, J. F. & Cloetens, P. (2012). *J. Struct. Biol.* **177**, 239–247.
- Kottler, C., David, C., Pfeiffer, F. & Bunk, O. (2007). *Opt. Express*, **15**, 1175–1181.
- Lombi, E., de Jonge, M. D., Donner, E., Ryan, C. G. & Paterson, D. (2011). *Anal. Bioanal. Chem.* **400**, 1637–1644.
- Medjoubi, K., Bucaille, T., Hustache, S., Béar, J.-F., Boudet, N., Clemens, J.-C., Delpierre, P. & Dinkespiler, B. (2010). *J. Synchrotron Rad.* **17**, 486–495.
- Menzel, A., Kewish, C. M., Kraft, P., Henrich, B., Jefimovs, K., Vila-Comamala, J., David, C., Dierolf, M., Thibault, P., Pfeiffer, F. & Bunk, O. (2010). *Ultramicroscopy*, **110**, 1143–1147.
- Mimura, H., Handa, S., Kimura, T., Yumoto, H., Yamakawa, D., Yokoyama, H., Matsuyama, S., Inagaki, K., Yamamura, K., Sano, Y., Tamasaku, K., Nishino, Y., Yabashi, M., Ishikawa, T. & Yamauchi, K. (2009). *Nat. Phys.* **6**, 122–125.
- Mukaide, T., Takada, K., Watanabe, M., Noma, T. & Iida, A. (2009). *Rev. Sci. Instrum.* **80**, 033707.
- Poirier, S., Maréchal, C., Ounsy, M., Buteau, A., Martinez, P., Gagey, B., Pierrot, P., Mederbel, M. & Rochat, J. M. (2009). *Proceedings of the 12th International Conference on Accelerator and Large Experimental Physics Control Systems (ICALPECS2009)*, Kobe, Japan.
- Ryan, C. G., Kirkham, R., Hough, R. M., Moorhead, G., Siddons, D. P., de Jonge, M. D., Paterson, D. J., de Geronimo, G., Howard, D. L. & Cleverley, J. S. (2009). *Nucl. Instrum. Methods Phys. Res. A*, **619**, 37–43.
- Somogyi, A., Kewish, C. M., Polack, F. & Moreno, T. (2011). *AIP Conf. Proc.* **1365**, 57–60.
- Vila-Comamala, J., Gorelick, S., Färm, E., Kewish, C. M., Diaz, A., Barrett, R., Guzenko, V. A., Ritala, M. & David, C. (2011). *Opt. Express*, **19**, 175–184.
- Yan, H., Kang, H. C., Conley, R., Liu, C., Macrander, A. T., Stephenson, G. B. & Maser, J. (2010). *X-ray Opt. Instrum.* **2010**, 401854.
- Yan, H., Rose, V., Shu, D., Lima, E., Kang, H. C., Conley, R., Liu, C., Jahedi, N., Macrander, A. T., Stephenson, G. B., Holt, M., Chu, Y. S., Lu, M. & Maser, J. (2011). *Opt. Express*, **19**, 15069–15076.